Asian Journal of Chemistry; Vol. 36, No. 10 (2024), 2375-2384

ASIAN JOURNAL OF CHEMISTRY

https://doi.org/10.14233/ajchem.2024.32404

# Structural, Magnetic and Electrochemical Properties of Nickel Manganese Ferrite ($Ni_xMn_{1-x}Fe_2O_4$) Nanoparticles Prepared *via* Coprecipitation Method

K.J. Oviya and P. Sivagurunathan*

Department of Physics, Annamalai University, Annamalai Nagar-608002, India

*Corresponding author: E-mail: sivagurunathanp2012@yahoo.com

*Received*: 26 July 2024; *Accepted*: 2 September 2024; *Published online*: 30 September 2024; AJC-21768

In current work, the co-precipitation approach was effectively used to synthesize $Ni_xMn_{1-x}Fe_2O_4$ nanoparticles. Thermal stability of the nickel manganese ferrite nanoparticle was observed at temperatures above 390 ºC by TG/DTA analysis. XRD investigation revealed the cubic structure of the synthesized $Ni_xMn_{1-x}Fe_2O_4$ nanoparticles. The average crystallite size of synthesized nanoparticles determined *via* Scherrer's equation, increases linearly with calcination temperature and nickel concentration. The FTIR spectra showed the existence of stretching vibrations of metal oxide, which are ascribed to the formation of nickel manganese ferrite nanoparticles. The surface morphology of $Ni_xMn_{1-x}Fe_2O_4$ nanoparticles, as observed using FESEM, exhibited a spherical shape. The EDX spectrum indicates the occurrence of Ni, Fe, Mn and O in the synthesized nickel manganese ferrite nanoparticles. The average size of the crystallites, as determined by XRD, closely matches the analysis conducted using HRTEM. The magnetic properties of $Ni_xMn_{1-x}Fe_2O_4$ nanoparticles were analyzed using VSM. Nickel manganese ferrite nanoparticles exhibit increasing saturation magnetization and coercivity values as nickel concentration increases, indicating soft ferrimagnetic properties and making it appropriate for high-density recording devices. The cyclic voltammetry investigation of $Ni_{0.7}Mn_{0.3}Fe_2O_4$ sample, calcinated at 600 ºC, reveals a significant specific capacitance of 590 F $g^{-1}$ at a scan rate of 2 mV $s^{-1}$, suggesting its potential use in supercapacitors.

**Keywords: Nickel manganese ferrite, Structural, Magnetic property, Electrochemical property.**

## INTRODUCTION

The development of spinel ferrite is relatively rapid and it is currently a more appealing material because of its nanometer level size. Recent advancements in the spinel ferrite development and use have yielded impressive outcomes [1,2]. Spinel ferrites are widely employed in technology because of their unique magnetic and electrochemical characteristics. Spinel ferrite compounds are used to manufacture electronic sensors, supercapacitors, memory devices, MRI devices and multilayer chip inductors [3]. The fluctuation of transition metal cations would play an important part in the modification of lattice structure, which modifies the magnetic and electrochemical characteristics of the materials. Distribution of the cation and dopants has a major impact on saturation magnetization, magnetic moment and other physical parameters [4].

Nickel ferrite ($NiFe_2O_4$) is a soft ferrite and possesses an inverse spinel structure, with $Ni^{2+}$ ions in the B site and $Fe^{3+}$ ions allocated evenly across both A and B sites [5]. The partial substitution of $MnFe_2O_4$ by divalent transition metal ions ($Ni^{2+}$, $Cu^{2+}$, $Zn^{2+}$, $Cd^{2+}$, *etc.*) yields extraordinary characteristics. Manganese ferrite, $MnFe_2O_4$, is a soft ferrite with a mixed spinel crystal structure in which $Mn^{2+}$ and $Fe^{3+}$ ions occupy both the A and the B sites. The substitution of $Ni^{2+}$ ions in $MnFe_2O_4$ alters its magnetic and electrochemical characteristics [6]. The enhanced magnetic characteristics of mixed nickel manganese ferrites make them fascinating materials with potential as soft magnets. The characteristics of ferrite nanoparticle are influenced by their chemical composition and production process [7]. A thorough review of the literature on various synthesis methods for the preparation of nickel manganese ferrite nanoparticles reveals that chemical methods frequently provide improved homogeneity and consistency in particle size and distribution [8]. However, such nanoferrites can also synthesized by various methods like co-precipitation [9], hydrothermal [10], solvothermal [11], ball milling [12] and oxalate precursor route [13]. Among those mentioned techniques, the co-precipitation method has the benefits of simplicity in preparation, adaptability

in composition, uniformity and affordability. An attempt has been made to synthesize $Ni_xMn_{1-x}Fe_2O_4$ ($x = 0.3, 0.5, 0.7$) nanoparticles using the co-precipitation technique and characterized.

## EXPERIMENTAL

Metal nitrates were used as precursors, sodium hydroxide as a precipitating agent and distilled water as a solvent in the synthesis of $Ni_xMn_{1-x}Fe_2O_4$ nanoparticles. For this work, pure AR grade (99%) iron, manganese and nickel nitrates were procured from Merck Chemicals Ltd. and used without additional purifications.

**Synthesis:** $Ni_xMn_{1-x}Fe_2O_4$ nanoparticles were synthesized using a simple co-precipitation technique [14]. Nickel and manganese concentrations "*x*" were adjusted from 0.3, 0.5 and 0.7 to get the desired results in nickel manganese ferrite. At optimum stoichiometric proportions, iron, manganese and nickel nitrates were dissolved in 30 mL of double-distilled water. After complete dissolution, precursor metal nitrate solutions were combined to maintain a (nickel + manganese)/ferrite ratio of 1:2 and stirred magnetically. Adding the appropriate amount of NaOH as a precipitating agent till the solution's pH become 9 and was maintained throughout the synthesis process. At 60 ºC, the solution was again magnetically stirred for 2 h. The brown sediment was eventually achieved and repeatedly washed with the required amount of acetone and double distilled water. The sediment was dried in a hot air oven at 100 ºC to obtain nickel manganese ferrite residue, which was then finely ground with an agate mortar. The prepared samples were calcined at 400, 500 and 600 ºC for 3 h.

## RESULTS AND DISCUSSION

**Thermal analysis:** To analyze the thermal characteristics of the synthesized $Ni_xMn_{1-x}Fe_2O_4$ nanoparticles, simultaneous thermal gravimetric and differential thermal analysis were conducted under a nitrogen atmosphere with the heating rate set at 20 ºC/min as depicted in Fig. 1. Three weight losses were identified in the TG curve. The first major weight loss (9%) occurs at temperatures below 200 ºC as a result of vaporization of water molecules. The second, meager weight loss was due to the breakdown of organic templates and observed within the temperature range of 200 to 250 ºC (4%). The final moderate

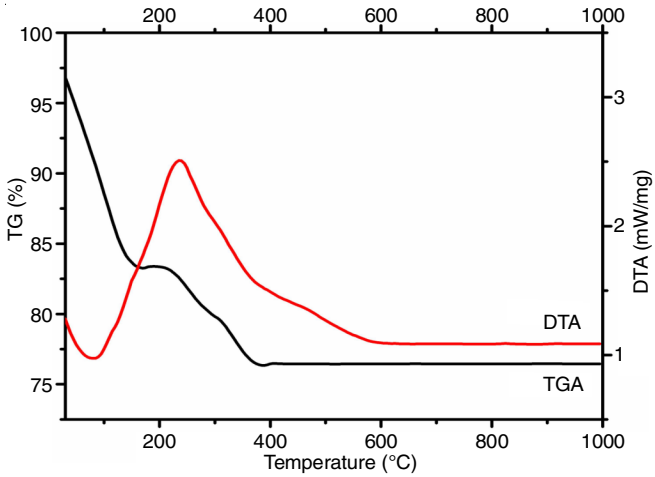


Fig. 1. TG/DT analysis of the as-synthesized $Ni_xMn_{1-x}Fe_2O_4$

loss of 6% between 250 and 390 ºC was attributed to the crystallization of the product. No further weight loss has been observed beyond 390 ºC, indicating the stable formation of nickel manganese ferrite nanoparticles [15]. In DTA curve, an endothermic peak at 110 ºC was caused by the loss of water content while the exothermic peak at 280 ºC was accompanied by the decomposition of the metal hydroxides [16]. This study highlights the necessity of calcination in the formation process of nickel manganese ferrite nanoparticles.

**XRD studies:** The phase identification and structural characterization of as-prepared and calcined nickel manganese ferrite nanoparticles were carried out by XRD technique. Fig. 2 depicts the XRD patterns of as-prepared and calcined $Ni_xMn_{1-x}Fe_2O_4$ ($x = 0.3, 0.5, 0.7$) at 400, 500 and 600 ºC. The prepared sample was amorphous and does not exhibit any peaks, indicating the necessity of the calcination process for the formation of $Ni_xMn_{1-x}Fe_2O_4$ nanoparticles [17]. The XRD patterns of $Ni_{0.3}Mn_{0.7}Fe_2O_4$, $Ni_{0.5}Mn_{0.5}Fe_2O_4$ and $Ni_{0.7}Mn_{0.3}Fe_2O_4$ nanoparticles calcined at 400, 500 and 600 ºC have an ordered structure indicating that the prepared nanoparticles are well crystalline. In addition, the observed peak intensity and width of nickel manganese ferrite nanoparticles varied with the calcination temperature indicating the structural changes after the thermal treatment. The XRD patterns of all $Ni_xMn_{1-x}Fe_2O_4$ nanoparticles exhibit distinct corresponding to the (220), (311), (222), (400), (422), (511) and (440) planes confirming single phase cubic

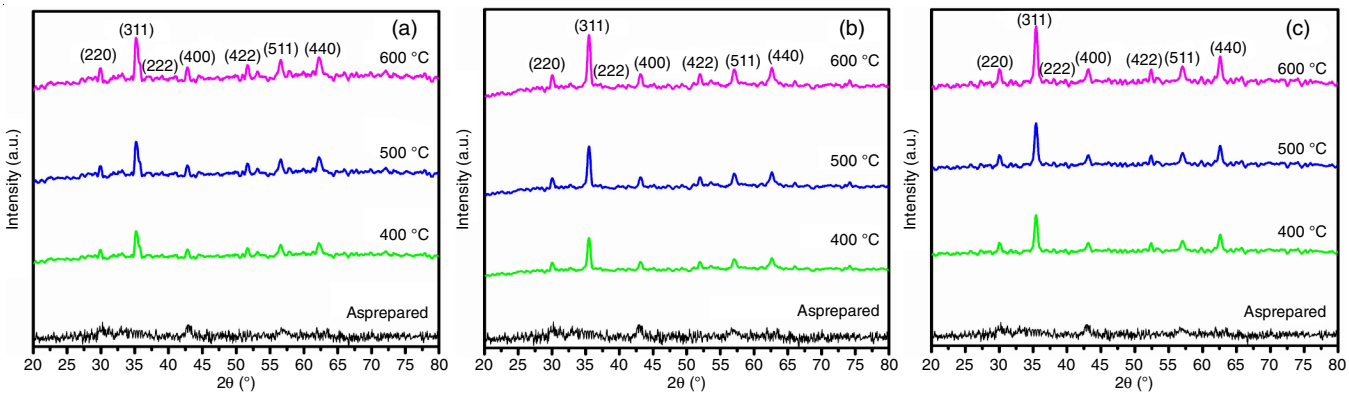


Fig. 2. (a), (b), (c) XRD spectra of as-prepared and calcinated $Ni_xMn_{1-x}Fe_2O_4$ ($x = 0.3, 0.5, 0.7$) nanoparticles at 400, 500 and 600 °C

spinel structure of nanoparticles. The indexing result corresponds well with the standard characteristic peaks of JCPDS, File No. # 74-2403 for $MnFe_2O_4$ and JCPDS, File No. # 19-629 for $NiFe_2O_4$ [18].

The average crystallite size of synthesized $Ni_xMn_{1-x}Fe_2O_4$ nanoparticles were determined using the Debye-Scherrer's formula [19]:

$$D = \frac{K\lambda}{\beta\cos\theta} \quad (1)$$

where D = average size of crystallites, K = 0.98, λ = X-ray wavelength (1.540 Å), β = full width at half maximum and θ = angle of diffraction.

The average lattice parameter 'a' was calculated using the formula [20]:

$$a = d_{hkl}\sqrt{h^2 + k^2 + l^2} \quad (2)$$

where, d = interplanar spacing; h, k, l = Miller indices.

The crystallite sizes and lattice parameters obtained for the $Ni_{0.3}Mn_{0.7}Fe_2O_4$, $Ni_{0.5}Mn_{0.5}Fe_2O_4$ and $Ni_{0.7}Mn_{0.3}Fe_2O_4$ at 400, 500 and 600 ºC are tabulated in Table-1, which reveals that as the calcination temperatures and nickel concentration increase, there is a corresponding increment in the crystallite size of nickel manganese ferrite nanoparticles. The crystallite size of the nanoferrites calcined from 400 to 600 ºC are 16, 19 and 22 nm respectively, indicating a linear correlation between the crystallite size and calcination temperature. The increase in size as the calcination temperature increase is attributed to the growth of the $Ni_xMn_{1-x}Fe_2O_4$ nanoparticles. Similar findings were observed for nanoparticles of $Ni_{0.5}Mn_{0.5}Fe_2O_4$ and $Ni_{0.7}Mn_{0.3}Fe_2O_4$ at various temperatures [21]. The increase of crystallite size with an increment in calcination temperature is due to the reduced stress within the unit cell, enabling atoms to occupy their designated lattice sites [22]. A similar trend is observed for $Ni_{0.3}Mn_{0.7}Fe_2O_4$, $Ni_{0.5}Mn_{0.5}Fe_2O_4$ and $Ni_{0.7}Mn_{0.3}Fe_2O_4$ nanoparticles calcined at 500 ºC and 600 ºC [23]. From Table-1, it was also evident that when the content of nickel increases, the lattice parameter decreases as well as increases with higher calcination temperatures. The lattice parameters of $Ni_{0.3}Mn_{0.7}Fe_2O_4$ nanoparticles calcined from 400 to 600 ºC are 8.350 Å, 8.365 Å and 8.384 Å. The increase in lattice constants with calcination temperature might be due to the structural rearrangements within the nickel manganese ferrite [24]. A similar trend is observed for all the prepared nickel ferrite nanoparticles at different temperatures. The lattice parameters for all the three prepared nanoparticles were 8.350 Å, 8.331 Å and 8.312 Å calcined at 400 ºC. The decrease of lattice constants with increasing nickel concentrations is mainly attributed to the exchange of a lesser ionic radius of $Ni^{2+}$ (0.69 Å) by a greater ionic radius of $Mn^{2+}$ (0.80 Å) cation [25]. Based on the XRD analysis, the current work suggested that the synthesized nickel manganese ferrites calcined at 600 ºC provide adequate insights into the structural, magnetic and electrochemical characteristics.

**FTIR studies:** FTIR spectra of the synthesized nickel manganese ferrites calcined at 600 ºC obtained in the range of frequency 4000-400 $cm^{-1}$ by KBr pellet technique through the solid phase is shown in Fig. 3. The absorption bands observed in the 600-400 $cm^{-1}$ range are indicative of the stretching vibrations of the tetrahedral and octahedral sites (A and B sites) of ferrite nanoparticles, as shown in Table-2. The absorption peak $\nu_1$ is related to stretching vibrations of Mn-O/Ni-O at the tetrahedral site; whereas the absorption peak $\nu_2$ is attributed to bond stretching vibrations induced by octahedral site metal and oxygen ions (Fe-O). In nickel manganese ferrite nanoparticles, the peaks observed around 538-530 $cm^{-1}$ and 435-423 $cm^{-1}$ indicate the high frequency band $\nu_1$ of tetrahedral Mn-O/Ni-O

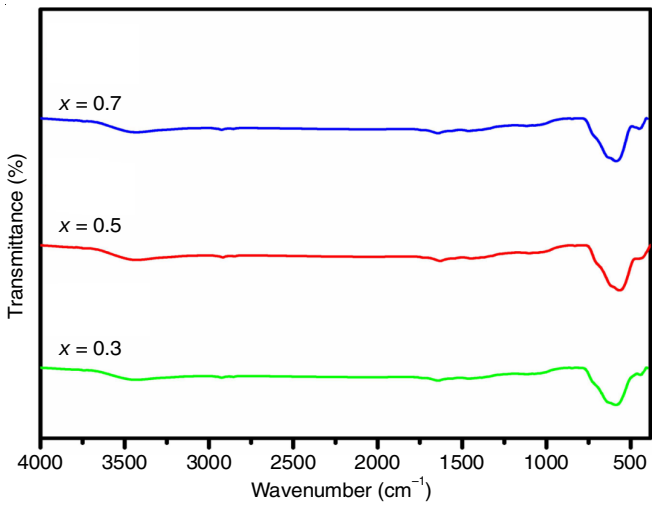


Fig. 3. FTIR spectra of $Ni_xMn_{1-x}Fe_2O_4$ ($x$ = 0.3, 0.5, 0.7) nanoparticles calcined at 600 °C

TABLE-1
STRUCTURAL ANALYSIS OF $Ni_xMn_{1-x}Fe_2O_4$ ($x$ = 0.3, 0.5, 0.7) NANOPARTICLES CALCINATED AT DIFFERENT TEMPERATURES WITH DIFFERENT CONCENTRATIONS

| Temperature (°C) | $Ni_{0.3}Mn_{0.7}Fe_2O_4$ | | $Ni_{0.5}Mn_{0.5}Fe_2O_4$ | | $Ni_{0.7}Mn_{0.3}Fe_2O_4$ | |
|---|---|---|---|---|---|---|
| | Particle size (nm) | a (Å) | Particle size (nm) | a (Å) | Particle size (nm) | a (Å) |
| 400 | 16 | 8.350 | 18 | 8.331 | 22 | 8.312 |
| 500 | 19 | 8.365 | 21 | 8.343 | 23 | 8.325 |
| 600 | 22 | 8.384 | 24 | 8.361 | 28 | 8.353 |

TABLE-2
ABSORPTION BAND OF $Ni_xMn_{1-x}Fe_2O_4$ ($x$ = 0.3, 0.5, 0.7) NANOPARTICLES CALCINATED AT 600 °C

| Temperature (°C) | $Ni_{0.3}Mn_{0.7}Fe_2O_4$ | | $Ni_{0.5}Mn_{0.5}Fe_2O_4$ | | $Ni_{0.7}Mn_{0.3}Fe_2O_4$ | |
|---|---|---|---|---|---|---|
| | $\nu_1$ ($cm^{-1}$) | $\nu_2$ ($cm^{-1}$) | $\nu_1$ ($cm^{-1}$) | $\nu_2$ ($cm^{-1}$) | $\nu_1$ ($cm^{-1}$) | $\nu_2$ ($cm^{-1}$) |
| 600 | 530 | 423 | 533 | 428 | 538 | 435 |

groups and the lower frequency band $\nu_2$ of octahedral Fe-O groups [26]. Based on the FTIR results, it is evident that the prepared nanoparticles are pure nickel manganese ferrite.

**Morphological studies:** The surface morphology of nickel manganese ferrite nanoparticles calcined at 600 ºC was characterized by FESEM techniques. Figs. 4 [(a-c)], [(f-h)] and [(k-m)] show the FESEM images of $Ni_{0.3}Mn_{0.7}Fe_2O_4$, $Ni_{0.5}Mn_{0.5}Fe_2O_4$ and $Ni_{0.7}Mn_{0.3}Fe_2O_4$ with different magnifications respectively. The FESEM images indicated that the prepared nanoparticles are spherical and consisted of little agglomerations. Nickel manganese ferrite nanoparticles exhibit agglomeration due to the strong magnetic interaction between the nanoparticles [27]. Using EDX, the elemental compositions of the synthesized samples were identified. The EDX spectra and corresponding weight percentage of $Ni_{0.3}Mn_{0.7}Fe_2O_4$, $Ni_{0.5}Mn_{0.5}Fe_2O_4$ and $Ni_{0.7}Mn_{0.3}Fe_2O_4$ nanoparticles at 600 ºC are shown in Fig. 4 [(d,i,n] and [(e,j,o)]. The EDX spectra of the synthesized nanoparticles contain only O, Mn, Ni and Fe in nickel manganese ferrite nanoparticles, which indicate the purity of the synthesized nanoferrites [28].

The HRTEM images of nickel manganese ferrite nanoparticles calcined at 600 ºC with different magnifications are shown in Fig. 5. The HRTEM micrographs of $Ni_xMn_{1-x}Fe_2O_4$ ($x = 0.3, 0.5, 0.7$) samples showed that the dispersed particles are spherical with mild aggregation. Fig. 5d,i,n displays the selected area electron diffraction pattern of $Ni_{0.3}Mn_{0.7}Fe_2O_4$, $Ni_{0.5}Mn_{0.5}Fe_2O_4$ and $Ni_{0.7}Mn_{0.3}Fe_2O_4$ nanoparticles. The SAED analysis reveals the polycrystalline nature of nickel manganese ferrite nanoparticles with discrete diffraction rings, which correspond to the (220), (311), (222), (400), (422) and (511) crystallographic planes of the nickel manganese ferrite structure obtained from XRD [29]. The distribution of particle size shown in Fig. 5e,j,o was determined by enumerating the particles in the images. The HRTEM image of $Ni_{0.3}Mn_{0.7}Fe_2O_4$, $Ni_{0.5}Mn_{0.5}Fe_2O_4$ and $Ni_{0.7}Mn_{0.3}Fe_2O_4$ nanoparticles, which showed a particle size of 24, 27 and 31 nm, respectively, is consistent with the finding obtained from XRD investigation [30].

**Magnetic properties:** The room temperature magnetic characteristics of the prepared $Ni_xMn_{1-x}Fe_2O_4$ ($x = 0.3, 0.5, 0.7$) samples were investigated by the VSM technique by applying a magnetic field spanning from 15 to +15 kOe. The M-H curves of $Ni_xMn_{1-x}Fe_2O_4$ ($x = 0.3, 0.5, 0.7$) samples calcined at 600 ºC are depicted in Fig. 6.

Even in high-field regions, the magnetization curves of $Ni_xMn_{1-x}Fe_2O_4$ ($x = 0.3, 0.5, 0.7$) samples are not fully saturated and the hysteresis pattern observed suggests that the material

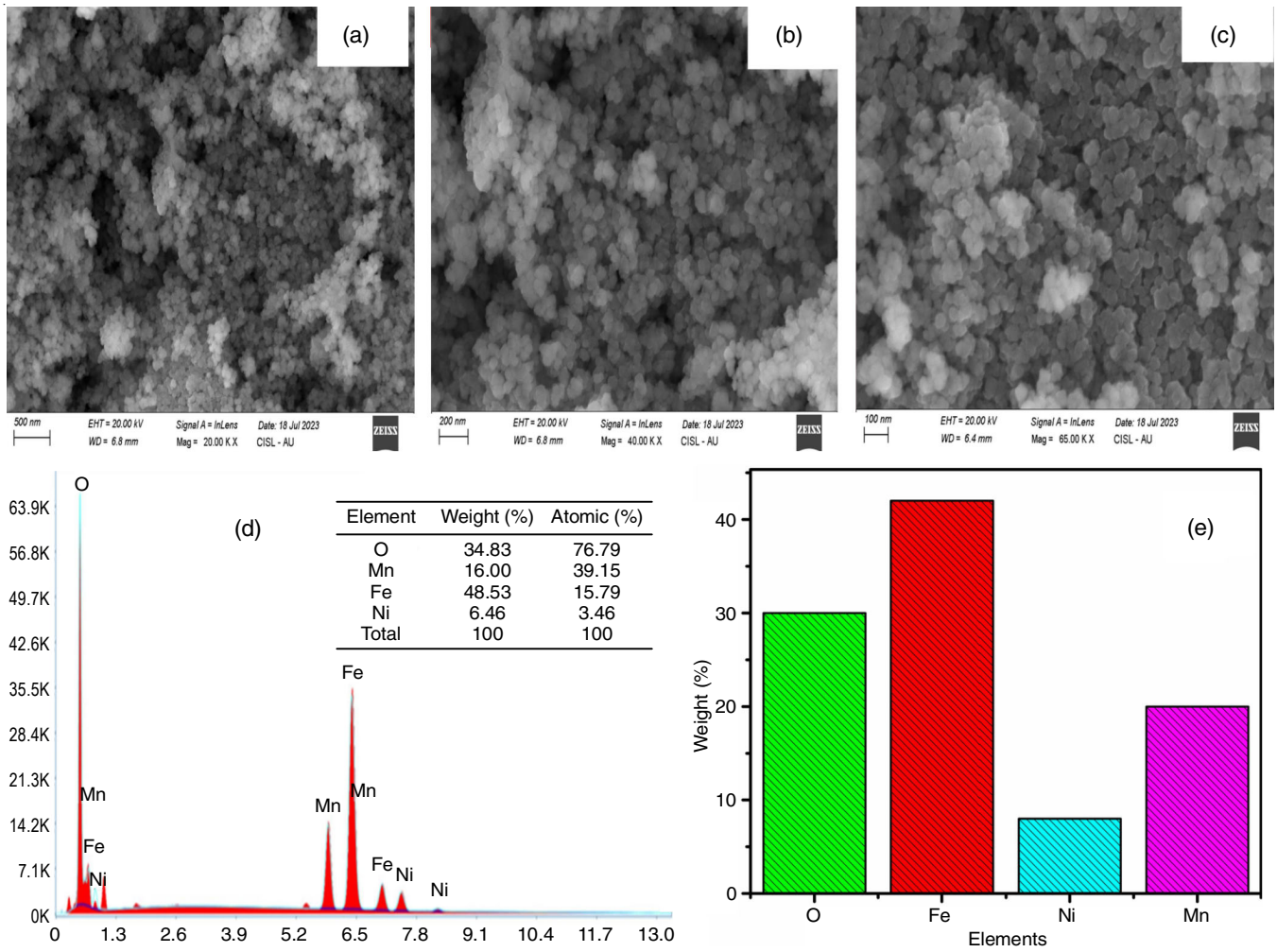


Fig. 4. (a), (b), (c), FESEM image of $Ni_{0.3}Mn_{0.7}Fe_2O_4$ nanoparticles calcinated at 600 °C with different magnifications, (d) corresponding EDX and (e) quantitative results

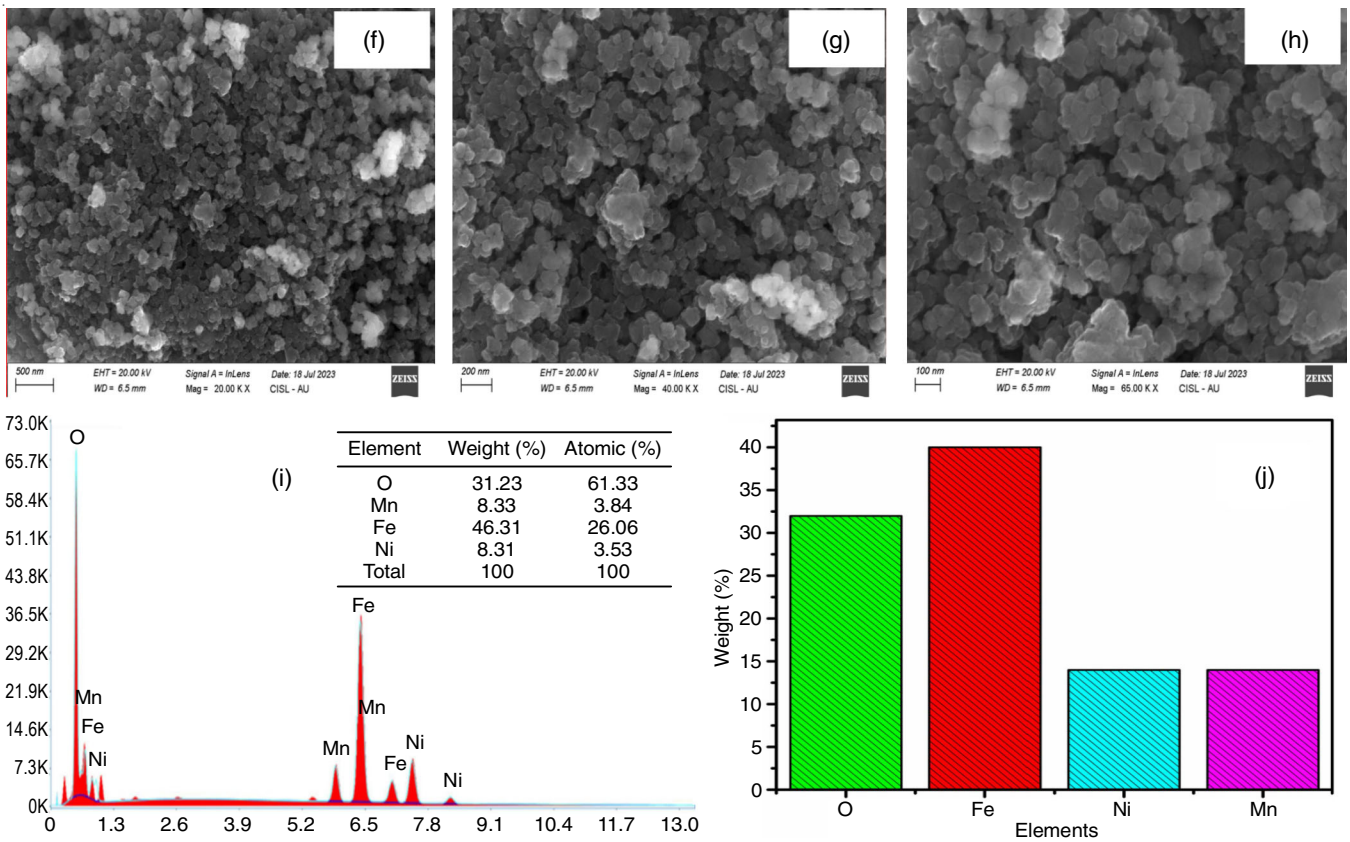


Fig. 4. (f), (g), (h), FESEM image of $Ni_{0.5}Mn_{0.5}Fe_2O_4$ nanoparticles calcinated at 600 °C with different magnifications, (i) corresponding EDX and (j) quantitative results

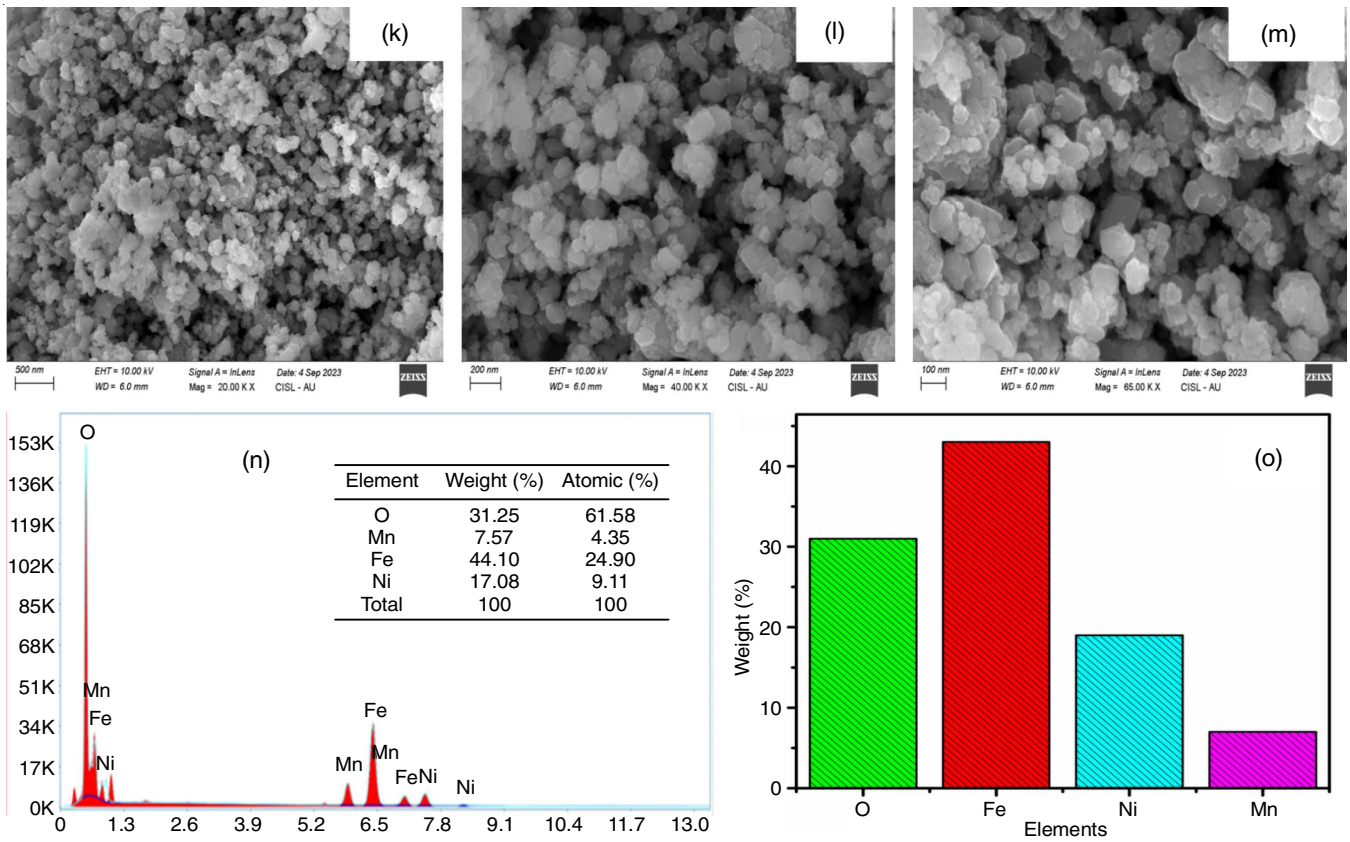


Fig. 4. (k), (l), (m), FESEM image of $Ni_{0.7}Mn_{0.3}Fe_2O_4$ nanoparticles calcinated at 600 °C with different magnifications, (n) corresponding EDX and (o) quantitative results

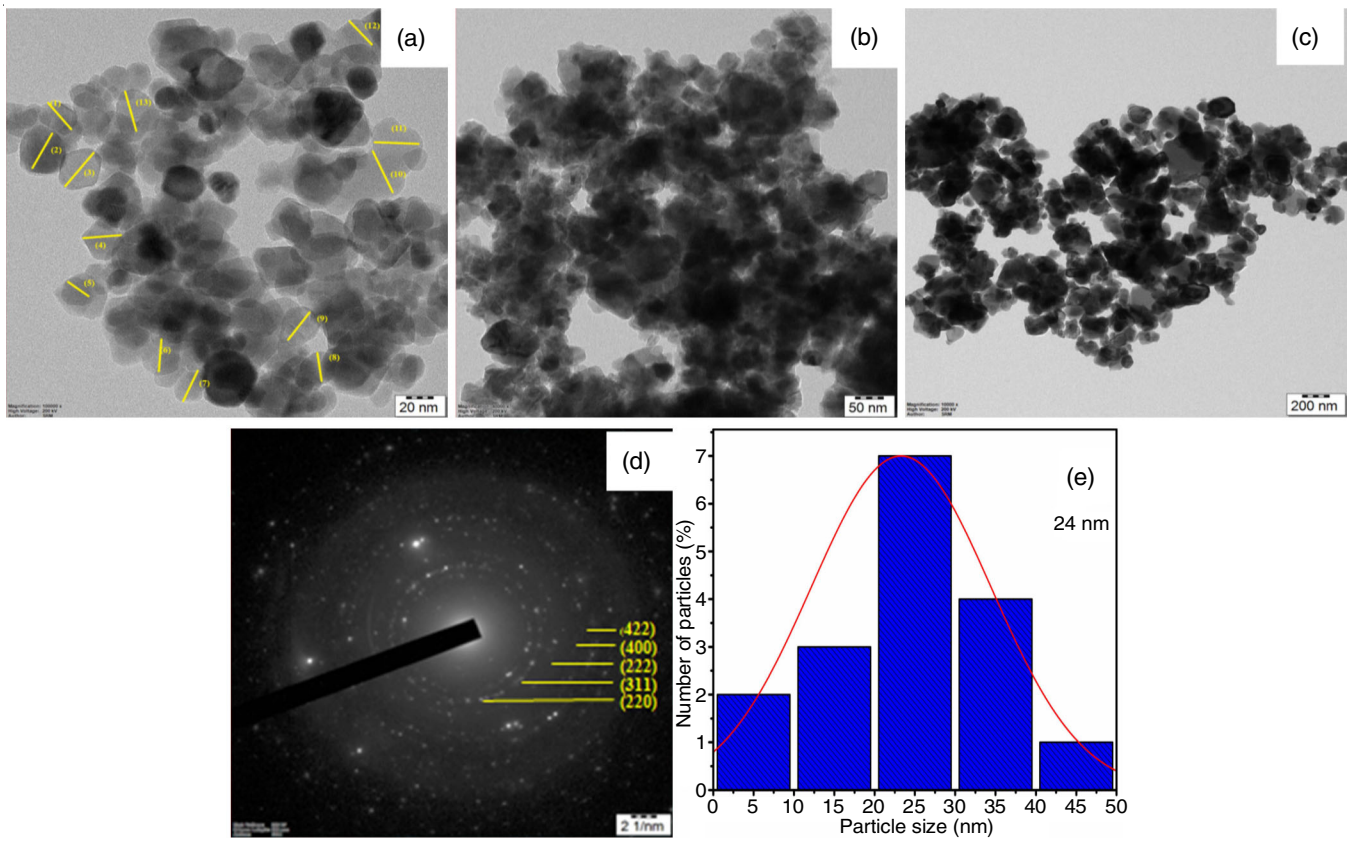


Fig. 5. (a), (b), (c), HRTEM micrographs of $Ni_{0.3}Mn_{0.7}Fe_2O_4$ nanoparticles calcinated at 600°C with different magnification and (d) SAED, (e) corresponding particle size distribution histogram

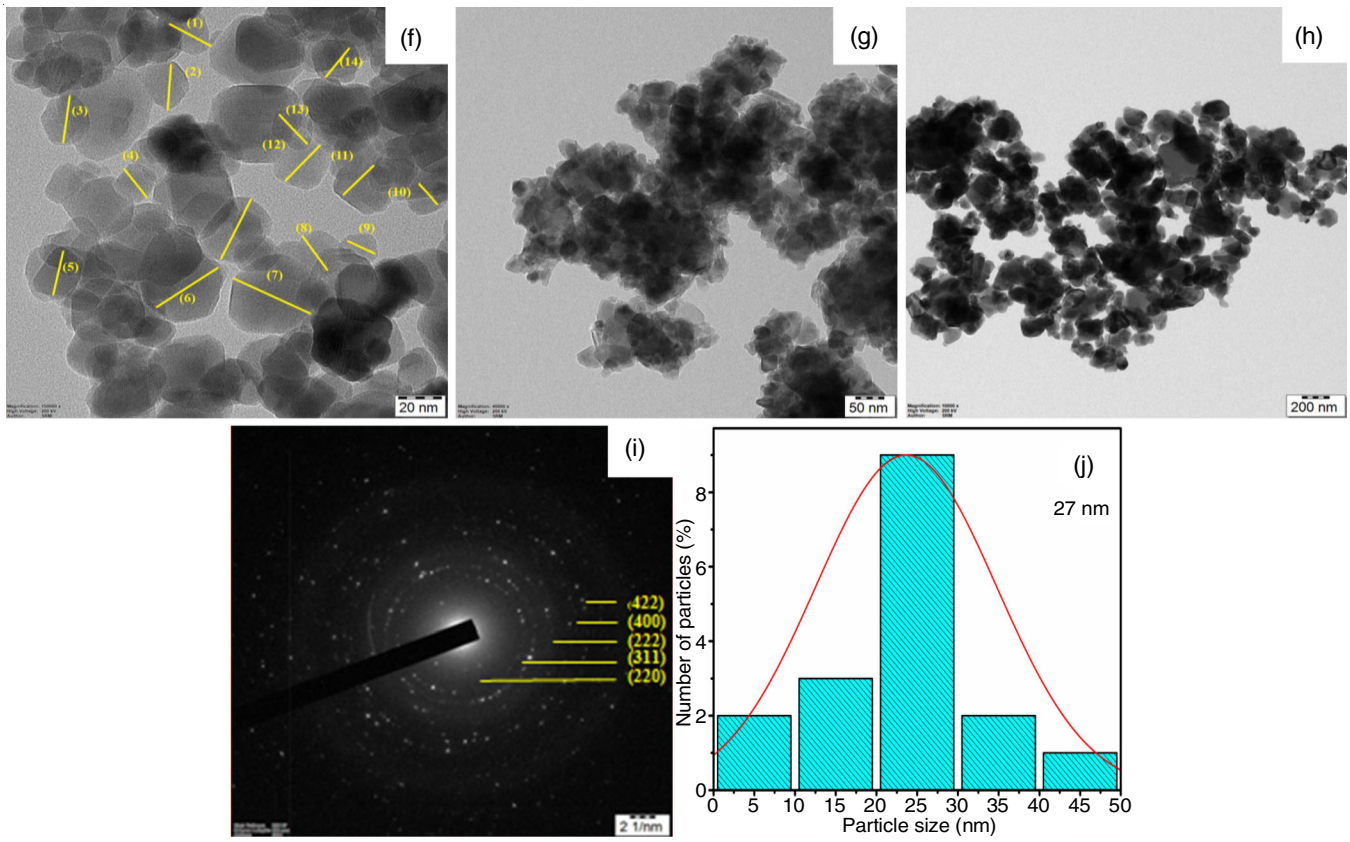


Fig. 5. (f), (g), (h), HRTEM micrographs of $Ni_{0.5}Mn_{0.5}Fe_2O_4$ nanoparticles calcinated at 600°C with different magnification and (i) SAED, (j) corresponding particle size distribution histogram

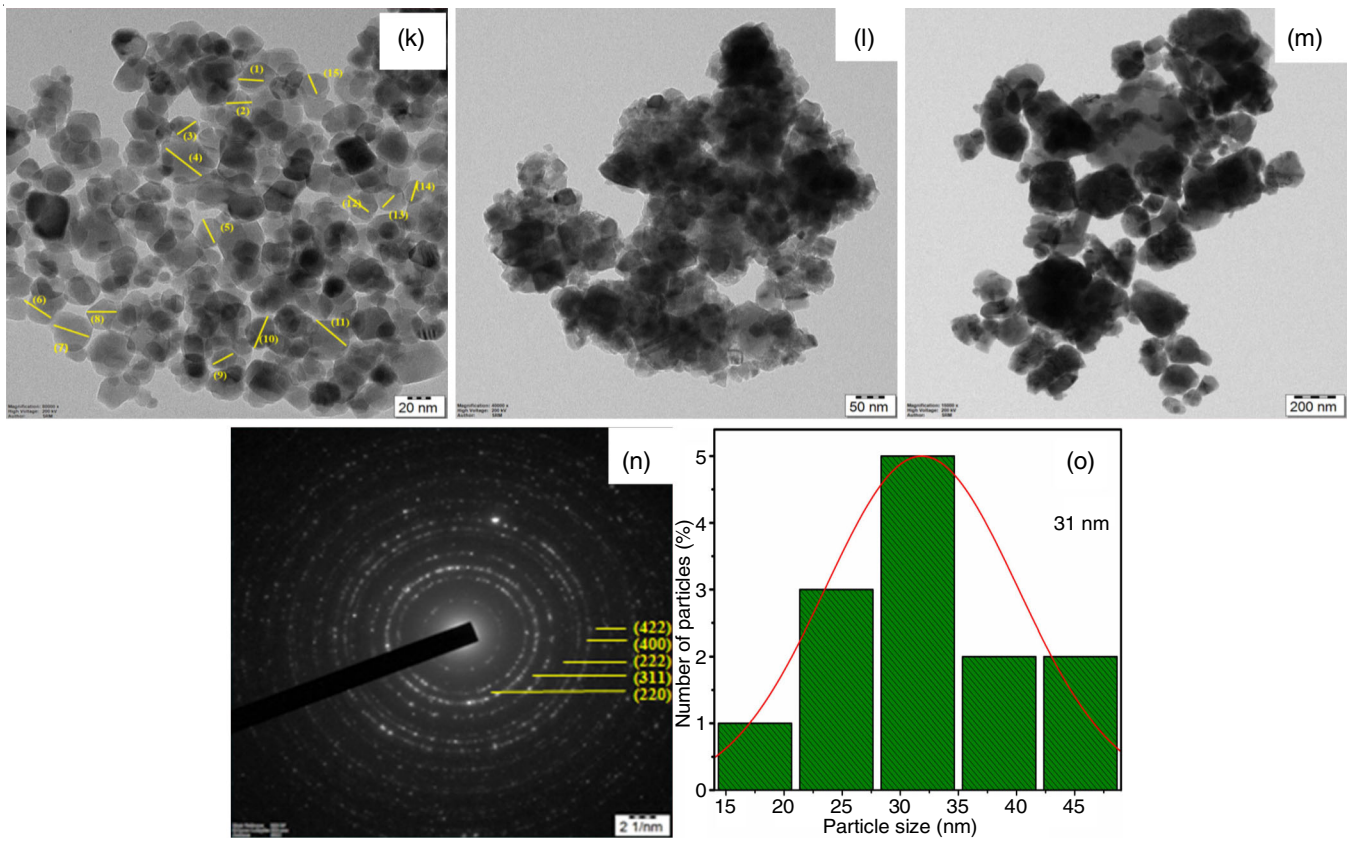


Fig. 5. (k), (l), (m), HRTEM micrographs of $Ni_{0.7}Mn_{0.3}Fe_2O_4$ nanoparticles calcinated at 600°C with different magnification and (n) SAED, (o) corresponding particle size distribution histogram

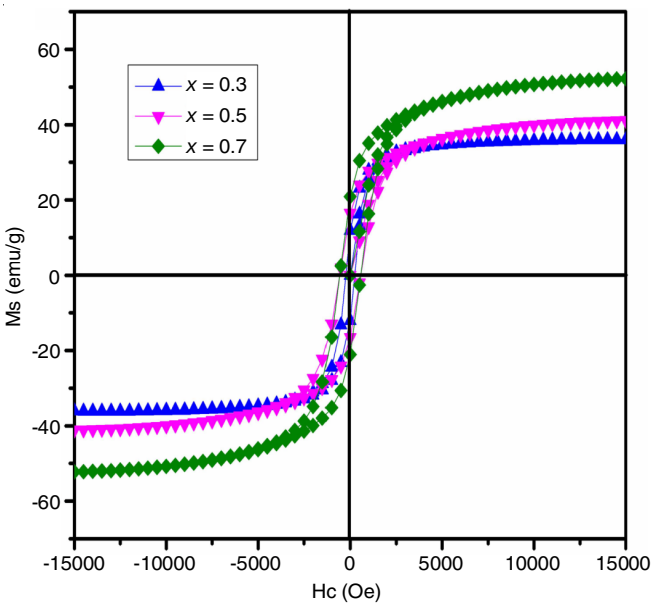


Fig. 6. Room temperature M-H curves of $Ni_xMn_{1-x}Fe_2O_4$ ($x = 0.3, 0.5, 0.7$) nanoparticles calcined at 600 °C

is ferrimagnetic in nature [31]. The unsaturation of magnetization is attributed to the disorder spins at the surface of the nanoparticles [32]. In spinel ferrites, the magnetic ions within the A and B sub-lattices interact in three ways: A-B, A-A and B-B interactions. Out of these, the A-B interactions show a greater impact relative to other interactions. The variations of magnetic saturation with nickel content can be interpreted using the Neel model. As per model, the total magnetizations of the sub-lattices B and A, referred to as $\Sigma M_B$ and $\Sigma M_A$, respectively, are antiparallel. The difference between the magnetization of the two sub-lattices represents $Ni_xMn_{1-x}Fe_2O_4$ ($x = 0.3, 0.5, 0.7$) samples *i.e.* $Ms = \Sigma M_{B\text{-sites}} - \Sigma M_{A\text{-sites}}$ [33]. The saturation magnetization (Ms) and coercivity (Hc) values of the synthesized $Ni_xMn_{1-x}Fe_2O_4$ ($x = 0.3, 0.5, 0.7$) samples are given in Table-3.

TABLE-3
SATURATION MAGNETIZATION (Ms) AND COERCIVITY (Hc) OF $Ni_xMn_{1-x}Fe_2O_4$ ($x = 0.3, 0.5, 0.7$) NANOPARTICLES CALCINATED AT 600 °C

| Sample | Ms (emu/g) | Hc (Oe) |
|---|---|---|
| $Ni_{0.3}Mn_{0.7}Fe_2O_4$ | 35 | 133 |
| $Ni_{0.5}Mn_{0.5}Fe_2O_4$ | 40 | 162 |
| $Ni_{0.7}Mn_{0.3}Fe_2O_4$ | 50 | 230 |

The saturation magnetization determined by extrapolating the high field magnetization curve are 35, 40 and 50 emu/g, with coercivity values of 133, 162 and 230 Oe, respectively [34]. In spinel ferrites, the magnetization primarily arises from super exchange interactions occurring between metal ions in A and B sites. Nickel ferrite has an inverse spinel structure, where $Ni^{2+}$ ions exhibit a preference for octahedral sites and $Fe^{3+}$ ions show an equal affinity for both tetrahedral and octahedral sites. Manganese ferrite has a mixed spinel structure and it can be represented as $(Mn_{1-x}Fe_x)[Mn_xFe_{1-x}]O_4$ where paren-

theses and brackets denote the tetrahedral and octahedral sites (A and B sites) and $x$ representing the inversion parameter. Here both $Mn^{2+}$ and $Fe^{3+}$ ions are suited within both the tetrahedral and octahedral sites [35]. Introducing nickel at a concentration of $x = 0.3$ into manganese ferrite nanoparticles results in $Ni^{2+}$ ions occupying octahedral sites, displacing some of $Mn^{2+}$ ions to tetrahedral sites, thereby enhancing saturation magnetization. Likewise, as the nickel concentration is increased from 0.3 to 0.5 and then to 0.7, an increased number of $Ni^{2+}$ ions occupy octahedral sites, causing more $Mn^{2+}$ ions to migrate to tetrahedral sites, consequently boosting magnetization. This leads to a decrease in the strength of the Mn-O-Fe interaction compared to the Fe-O-Fe and Ni-O-Fe interactions. The contribution of $Ni^{2+}$ ions in $Ni_xMn_{1-x}Fe_2O_4$ nanoparticles strengthens the spin orbit coupling, hence the anisotropy and coercivity increase [36]. In this study, the observed crystallite sizes for various nickel concentrations at 600 ºC are 22, 24 and 28 nm. These sizes are significantly lesser than the critical size of 42 nm behaving as single magnetic domains [37]. Furthermore, an increment in coercivity values and crystallite size with increasing nickel concentrations, confirms the single-domain nature of the prepared nickel manganese ferrite nanoparticles [38]. The linear enhancement of magnetic saturation and coercivity values with increased nickel content in $Ni_xMn_{1-x}Fe_2O_4$ obtained in this work indicates its suitability for high-density recording media.

**Cyclic voltammetry:** The electrochemical measurements of $Ni_xMn_{1-x}Fe_2O_4$ ($x = 0.3, 0.5, 0.7$) electrodes have between 2 mV/s and 100 mV/s, covering the potential range 0 to 0.5 V as depicted in Fig. 7a-c. Initially, at a scanning rate of 2 mV/s, the CV curve displays a characteristic rectangular shape. However, as the scan rates increase, the pattern of the cyclic voltammograms changes, revealing the Faradaic currents produced through the reduction and oxidation of specific chemically active substances at the electrode. As a result, two peaks become apparent in the cyclic voltammograms: an oxidation peak during the '+ve' current and a reduction peak during the '-ve' current, thus confirming the pseudo-capacitive behaviour of the material [39]. These peaks migrate to higher and lower potentials with increasing scan rates.

The specific capacitance of $Ni_xMn_{1-x}Fe_2O_4$ electrode was calculated by employing eqn. 3 [40]:

$$C_s = \frac{Q}{m.\Delta V} \quad (3)$$

where Cs = the specific capacitance, Q = the anodic and cathodic response measured during each scan, m = the mass of electrode substance (mg) and ΔV = the difference in the potential window.

The electrochemical experiments were performed using a 0.1 M solution of KOH, employing a standard three-electrode configuration. This setup comprised the samples as the working electrode, an Ag/AgCl reference electrode and a high Pt wire acting as counter electrode [41]. The specific capacitance (Cs) values of $Ni_xMn_{1-x}Fe_2O_4$ ($x = 0.3, 0.5, 0.7$) samples calcined at 600 ºC with different scan rates are tabulated in Table-4.

TABLE-4
SPECIFIC CAPACITANCE VALUES OF $Ni_xMn_{1-x}Fe_2O_4$ ($x = 0.3, 0.5, 0.7$) NANOPARTICLES CALCINATED AT 600 °C WITH DIFFERENT SCAN RATES

| Scan rates (mV/s) | Specific capacitance (F/g) | | |
|---|---|---|---|
| | $Ni_{0.3}Mn_{0.7}Fe_2O_4$ | $Ni_{0.5}Mn_{0.5}Fe_2O_4$ | $Ni_{0.7}Mn_{0.3}Fe_2O_4$ |
| 2 | 482 | 511 | 590 |
| 5 | 301 | 379 | 412 |
| 10 | 103 | 129 | 167 |
| 20 | 89 | 95 | 100 |
| 30 | 60 | 67 | 72 |
| 40 | 40 | 48 | 55 |
| 50 | 24 | 31 | 39 |
| 100 | 13 | 15 | 17 |

The examination of $Ni_xMn_{1-x}Fe_2O_4$ ($x = 0.3, 0.5, 0.7$) at different concentrations reveals that as the nickel content increases in nickel manganese ferrite, there is a gradual increase in specific capacitance with varying scan rates. Moreover, the specific capacitance of$Ni_xMn_{1-x}Fe_2O_4$ ($x = 0.3, 0.5, 0.7$) decline as the scan rate increases from 2 mV/s to 100 mV/s. The study significantly demonstrates that the specific capacitance reaches its maximum value at lower scan rates. It's a well-established fact that the area under a cyclic voltammetry curve correlates directly with its specific capacitance. Consequently, across all the CV curves, it is apparent that the specific capacitance diminishes with higher scan rates. This decline can be attributed to the limited time available for electrolyte ions to fully diffuse into the nanopores of the electrode, where Faradaic reactions take place, at elevated scan rates. This limitation renders certain

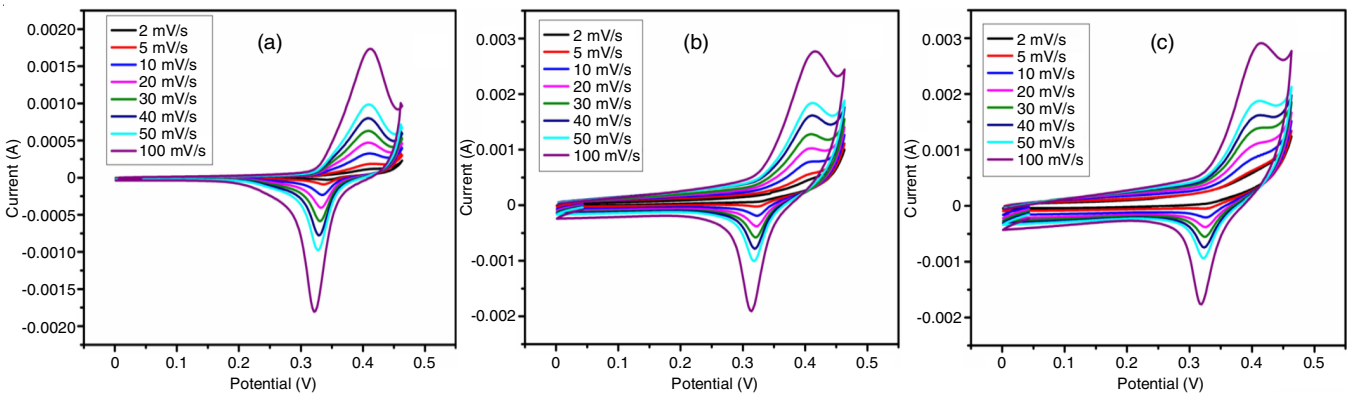


Fig. 7. (a-c) CV pattern of $Ni_xMn_{1-x}Fe_2O_4$ ($x = 0.3, 0.5, 0.7$) nanoparticles calcinated at 600 °C for different scan rates

portions of the active surface area inaccessible. Moreover, this phenomenon may be ascribed to the presence of significant ohmic resistance observed at higher scan rates [42]. Moreover, the observation of higher specific capacitance at lower scan rates suggests that ionic diffusion occurs on both internal and external surfaces. Conversely, the reduced 'Cs' values at greater scan rates imply that ionic diffusion predominantly occurs solely on the outer surfaces [43]. The specific capacitance determined through the electrochemical measurements indicated a significant increase in capacitance for $Ni_xMn_{1-x}Fe_2O_4$ ($x$ = 0.3, 0.5, 0.7) samples calcined at 600 ºC, with values increasing from 482 F/g, 511 F/g, to 590 F/g at a low scan rate of 2 mV/s for each respective sample. In comparison to the reported specific capacitance value of 424 F/g for $Ni_{0.5}Mn_{0.5}Fe_2O_4$ at a scan rate of 2 mV/s by Sreeja *et al.* [44] for the crystallite size of 50 nm at 700 ºC, the current work $Ni_{0.5}Mn_{0.5}Fe_2O_4$ showed a superior specific capacitance value of 511 F/g at a low scan rate of 2 mV/s for the crystallite size of 28 nm calcined at 600 ºC. Therefore, $Ni_{0.7}Mn_{0.3}Fe_2O_4$ sample revealed a higher specific capacitance value of 590 F/g at a low scan rate of 2 mV/s suggesting its potential for more effective applications in supercapacitors.

## Conclusion

The nickel manganese ferrite nanoparticles were successfully prepared by co-precipitation technique with different concentrations at various calcination temperatures. The structural, compositional, magnetic and electrochemical behaviour of the calcined samples was well studied. The TG/DTA study revealed the thermal stability of nickel manganese ferrite nanoparticles. The high crystallinity of the prepared $Ni_xMn_{1-x}Fe_2O_4$ nanoparticles was affirmed by the XRD patterns. The average crystallite size shows an increasing tendency for both calcination temperatures and increasing nickel concentration whereas the lattice constants decreased with an increase in nickel concentration. The FTIR spectra confirmed the functional groups present at the tetrahedral and octahedral sites, with absorption bands around 538-530 $cm^{-1}$ and 435-423 $cm^{-1}$. FESEM and HRTEM with SAED pattern confirmed the spherical shape of the synthesized sample and the EDX analysis revealed that the sample includes only oxygen, manganese, nickel and iron. The particle size determined from XRD using Debye-Scherer's formula was consistent with that calculated from HRTEM. The observed variation in magnetic saturation and coercivity values with an increase of nickel content in manganese ferrite revealed the ferrimagnetic behaviour of the synthesized nanoparticles and it is well suited for high density recording media. An enhanced capacitance value of 590 F/g was observed at a scan rate of 2 mV/s in the CV analysis, indicating its suitability for supercapacitor applications.

## ACKNOWLEDGEMENTS

The authors extended their gratitude to the Centralized Instrumentation and Service Laboratory and DST FIST II at Annamalai University for generously providing access to their research laboratory facilities.

## CONFLICT OF INTEREST

The authors declare that there is no conflict of interests regarding the publication of this article.

## REFERENCES

1. A. Hussain, T. Abbas and S.B. Niazi, *Ceram. Int.*, **39**, 1221 (2013); https://doi.org/10.1016/j.ceramint.2012.07.049
2. S. Gaffar, A. Kumar and U. Riaz, *J. Electroceram.*, **51**, 246 (2023); https://doi.org/10.1007/s10832-023-00333-x
3. L. Shao, A. Sun, Y. Zhang, L. Yu, N. Suo and Z. Zuo, *J. Mater. Sci. Mater. Electron.*, **32**, 20474 (2021); https://doi.org/10.1007/s10854-021-06557-3
4. S. Nazir, S. Sami, S. Haider, M. Shahid, M. Sher, M.F. Warsi, Q. Nadeem and M.A. Khan, *Ceram. Int.*, **42**, 13459 (2016); https://doi.org/10.1016/j.ceramint.2016.05.133
5. G.M. Al-Senani, F.F. Al-Fawzan, R.S. Almufarij, O.H. Abd-Elkader and N.M. Deraz, *Crystals*, **12**, 1542 (2022); https://doi.org/10.3390/cryst12111542
6. T.F. Marinca, I. Chicinas, O. Isnard and B.V. Neamtu, *Ceram. Int.*, **42**, 4754 (2016); https://doi.org/10.1016/j.ceramint.2015.11.155
7. B.I. Kharisov, H.V. Rasika Dias and O.V. Kharissova, *Arabian J. Chem.*, **12**, 1234 (2019); https://doi.org/10.1016/j.arabjc.2014.10.049
8. S. Ramesh, B. Dhanalakshmi, B. Chandra Sekhar, P.S.V. Subba Rao and B. Parvatheeswara Rao, *Appl. Phys.*, **122**, 1 (2016); https://doi.org/10.1007/s00339-016-0517-6
9. B.V. Tirupanyam, C. Srinivas, S.S. Meena, S.M. Yusuf, A. Satish Kumar, D.L. Sastry and V. Seshubai, *J. Magn. Magn. Mater.*, **392**, 101 (2015); https://doi.org/10.1016/j.jmmm.2015.05.010
10. Z. Jabeen, A. Dawood, M. Alomar, S.N. Khan, I. Ali, M. Asif, W. Abbas, M.S. Irshad and M. Ahmad, *Surf. Interfaces*, **402**, 103130 (2023); https://doi.org/10.1016/j.surfin.2023.103130
11. B. Aslibeiki, P. Kameli, M.H. Ehsani, H. Salamati, E. Agostinelli, G. Muscas, V. Foglietti, S. Casciardi and D. Peddis, *J. Magn. Magn. Mater.*, **399**, 236 (2016); https://doi.org/10.1016/j.jmmm.2015.09.081
12. A. Hajalilou, M. Hashim, R. Ebrahimi-Kahrizsangi and H.M. Kamari, *J. Alloys Compd.*, **633**, 306 (2015); https://doi.org/10.1016/j.jallcom.2015.02.061
13. M.M. Hessien, Z.I. Zaki and A.Q. Mohsen, *Adv. Mater. Phys. Chem.*, **3**, 1 (2013); https://doi.org/10.4236/ampc.2013.31A001
14. D. Deivatamil, J.A.M. Mark, T. Raghavan and J.P. Jesuraj, *Inorg. Chem. Commun.*, **123**, 108355 (2021); https://doi.org/10.1016/j.inoche.2020.108355
15. R.S. Pandav, R.P. Patil, S.S. Chavan, I.S. Mulla and P.P. Hankare, *J. Magn. Magn. Mater.*, **417**, 407 (2016); https://doi.org/10.1016/j.jmmm.2016.04.090
16. H. Yang, L. Zhao, X. Yang, L. Shen, L. Yu, W. Sun, Y. Yan, W. Wang and S. Feng, *J. Magn. Magn. Mater.*, **271**, 230 (2004); https://doi.org/10.1016/j.jmmm.2003.09.030
17. E.R. Kumar, P.S.P. Reddy, G.S. Devi and S. Sathiyaraj, *J. Magn. Magn. Mater.*, **398**, 281 (2016); https://doi.org/10.1016/j.jmmm.2015.09.018
18. G. Mathubala, A. Manikandan, S.A. Antony and P. Ramar, *J. Mol. Struct.*, **1113**, 79 (2016); https://doi.org/10.1016/j.molstruc.2016.02.032
19. W. Pan, X. Zhang, Q.-F. Liu and J. Wang, *Soft Nanosci. Lett.*, **7**, 17 (2017); https://doi.org/10.4236/snl.2017.72002
20. M. Kurian and C. Kunjachan, *Int. Nano Lett.*, **4**, 73 (2014); https://doi.org/10.1007/s40089-014-0122-7
21. C. Barathiraja, A. Manikandan, A.M. Uduman Mohideen, S. Jayasree and S.A. Antony, *J. Supercond. Nov. Magn.*, **29**, 477 (2016); https://doi.org/10.1007/s10948-015-3312-2
22. N. Nazari, M.M. Golzan and K. Mabhouti, *Sci. Rep.*, **14**, 6407 (2024); https://doi.org/10.1038/s41598-024-57045-7

23. Y. Köseoglu, *Ceram. Int.*, **39**, 4221 (2013); https://doi.org/10.1016/j.ceramint.2012.11.004
24. N. Channa, M. Khalid, A.D. Chandio, G. Mustafa, M.S. Akhtar, J.K. Khan, J. Ahmad and K.A. Kalhoro, *J. Mater. Sci. Mater. Electron.*, **31**, 1661 (2020); https://doi.org/10.1007/s10854-019-02684-0
25. S.K. Jesudoss, J.J. Vijaya, L.J. Kennedy, P.I. Rajan, H.A. Al-Lohedan, R.J. Ramalingam, K. Kaviyarasu and M. Bououdina, *J. Photochem. Photobiol. B*, **165**, 121 (2016); https://doi.org/10.1016/j.jphotobiol.2016.10.004
26. R. Kesavamoorthi and C.R. Raja, *J. Supercond. Nov. Magn.*, **29**, 2729 (2016); https://doi.org/10.1007/s10948-016-3792-8
27. S. Mirzaee, Y. Azizian-Kalandaragh and P. Rahimzadeh, *Solid State Sci.*, **99**, 106052 (2020); https://doi.org/10.1016/j.solidstatesciences.2019.106052
28. J. Suresh, B. Trinadh, B.V. Babu, P.V.S.S.S.N. Reddy, B.S. Mohan, A.R. Krishna and K. Samatha, *Physica B*, **620**, 413264 (2021); https://doi.org/10.1016/j.physb.2021.413264
29. E.R. Kumar, A.S. Kamzin and T. Prakash, *J. Magn. Magn. Mater.*, **378**, 389 (2015); https://doi.org/10.1016/j.jmmm.2014.11.019
30. S. Yuvaraj, N. Manikandan and G. Vinitha, *Ceram. Int.*, **44**, 22592 (2018); https://doi.org/10.1016/j.ceramint.2018.09.033
31. T. Dippong, E.A. Levei, I.G. Deac, I. Petean and O. Cadar, *Int. J. Mol. Sci.*, **23**, 3097 (2022); https://doi.org/10.3390/ijms23063097
32. A.I. Saputra, Herdiman, E. Suharyadi, T. Kato and S. Iwata, *IOP Conf. Ser. Mater. Sci. Eng.*, **546**, 042041 (2019); https://doi.org/10.1088/1757-899X/546/4/042041
33. G. Asghar, E. Tariq, S.N. Khisro, G.H. Tariq, M.S. Awan, M.A.R. Khan, Y. Iqbal, K. Safeen and M. Anis-ur-Rehman, *Kuwait J. Sci.*, **50**, 518 (2023); https://doi.org/10.1016/j.kjs.2023.05.001
34. K.P. Chae, W.O. Choi, J.G. Lee, B.S. Kang and S.H. Choi, *J. Magn.*, **18**, 21 (2013); https://doi.org/10.4283/JMAG.2013.18.1.021
35. I. Chicinas, T.F. Marinca, B.V. Neamþu, F. Popa, O. Isnard and V. Pop, *IEEE Trans. Magn.*, **50**, 1 (2014); https://doi.org/10.1109/TMAG.2013.2285246
36. K. Sasikumar, R. Bharathikannan, G. Sujithkumar, G.J. Arputhavalli, S. Raja, M. Vidhya, R. Marnadu and R. Suresh, *J. Supercond. Nov. Magn.*, **34**, 2189 (2021); https://doi.org/10.1007/s10948-021-05948-1
37. Aakash, R. Choubey, D. Das and S. Mukherjee, *J. Alloys Compd.*, **668**, 33 (2016); https://doi.org/10.1016/j.jallcom.2016.01.198
38. L. Zhao, H. Yang, L. Yu, Y. Cui, X. Zhao and S. Feng, *J. Magn. Magn. Mater.*, **305**, 91 (2006); https://doi.org/10.1016/j.jmmm.2005.11.043
39. T.T.H. Hoang, S. Le The, S. Maenosono, T.N. Van, H.G. Do Thi, S.-E. Chun, T.T. Viet and N.T. Van, *J. Appl. Electrochem.*, **53**, 2109 (2023); https://doi.org/10.1007/s10800-023-01907-x
40. P. Sivagurunathan and S.R. Gibin, *J. Mater. Sci. Mater. Electron.*, **27**, 2601 (2016); https://doi.org/10.1007/s10854-015-4065-1
41. M.K. Zate, S.M.F. Shaikh, V.V. Jadhav, K.K. Tehare, S.S. Kolekar, R.S. Mane, M. Naushad, B.N. Pawar and K.N. Hui, *J. Anal. Appl. Pyrolysis*, **116**, 177 (2015); https://doi.org/10.1016/j.jaap.2015.09.012
42. S. Sharifi, A. Yazdani and K. Rahimi, *Sci. Rep.*, **10**, 10916 (2020); https://doi.org/10.1038/s41598-020-67802-z
43. P. Bhojane, A. Sharma, M. Pusty, Y. Kumar, S. Sen and P. Shirage, *J. Nanosci. Nanotechnol.*, **17**, 1387 (2017); https://doi.org/10.1166/jnn.2017.12666
44. S.B. Sreeja Lekshmi, S.R. Gibin, V.K. Premkumar and C. Rajeevgandhi, *Neuroquantology*, **20**, 936 (2022); https://doi.org/10.48047/NQ.2022.20.1.NQ22377